7-2010

Signal Modeling in the Far-Infrared Region for Nondestructive Evaluation Applicatinos

Chien-Ping T. Chiou
Iowa State University, cchiou@iastate.edu

David K. Hsu
Iowa State University

Daniel J. Barnard
Iowa State University, dbarnard@iastate.edu

Kwang-Hee Im
Iowa State University

R. Bruce Thompson
Iowa State University

SIGNAL MODELING IN THE FARINFRARED REGION FOR NONDESTRUCTIVE EVALUATION APPLICATIONS

ChienPing Chiou, David K. Hsu, Dan Barnard, KwangHee Im, and R. Bruce Thompson

Citation: AIP Conf. Proc. **1335**, 581 (2011); doi: 10.1063/1.3591903
View online: http://dx.doi.org/10.1063/1.3591903
View Table of Contents: http://proceedings.aip.org/dbt/dbt.jsp?KEY=APCPCS&Volume=1335&Issue=1
Published by the American Institute of Physics.

SIGNAL MODELING IN THE FAR-INFRARED REGION FOR NONDESTRUCTIVE EVALUATION APPLICATIONS

Chien-Ping Chiou, David K. Hsu, Dan Barnard, Kwang-Hee Im, and R. Bruce Thompson

Center for Nondestructive Evaluation, Iowa State University, Ames, Iowa 50011

ABSTRACT. Terahertz radiation (a.k.a. T-ray) has emerged as a powerful inspection technique in recent years. It extends into the lower region of far-infrared in the electromagnetic spectrum, and has been proven very effective in many NDE applications. T-ray is particularly useful in some areas where accessibility is difficult or even not possible for other conventional NDE methods. Here we report a modeling effort of T-ray signal in one such application: the detection of "hidden delamination", a special situation that a delamination was shadowed by another. This special case was experimentally simulated by two parallel saw-cuts in glass composites. In this paper, we also explore the feasibility of combing T-ray and Fourier transform infrared spectroscopy using a unified least-squares scheme for material characterization.

Keywords: Terahertz Radiation, Fourier Transform Infrared Spectroscopy, Delamination Evaluation, Signal Modeling, Material Characterization
PACS: 81.70.Ex

INTRODUCTION

Recently, Terahertz radiation (hereafter denoted as T-ray) has become a powerful NDE technique for inspection and material characterization (see, e.g. [1]). T-ray fills the "gap" in the lower far-infrared region of the electromagnetic spectrum, and complements existing techniques in higher frequency regions such as the Fourier transform infrared spectroscopy (FTIR). It is particularly effective in some areas where accessibility is difficult or even not possible for other conventional NDE methods. In these areas, modeling allows us to evaluate those problematic situations much more cost-effectively. Here we report a modeling effort of T-ray signals in several cases of "hidden delamination", where a delamination was shielded by another. This hidden delamination was experimentally simulated by two parallel saw-cut slots made into a glass fiber reinforced polyester (GFRP) plate. T-ray has also shown great potential in characterizing electromagnetic properties of materials. In this paper, we assess the feasibility of combing T-ray and FTIR using a unified least-squares scheme for material property inversion.

MODELING T-RAY SIGNALS THROUGH "HIDDEN DELAMINATION"

Fig. 1 shows the T-ray reflection scan of a GFRP plate, in which multiple circular saw cuts were made into the side of the plate to simulate delaminations (Fig. 1). For the double saw cuts on the left-hand side (Figs. 1b and 1c), we can see that the lower 4" cut would be "hidden" by the upper 5" cut ultrasonically, since ultrasound, as a mechanical wave, cannot get pass the air gap of the upper cut. However, T-ray, as an electromagnetic

Review of Progress in Quantitative Nondestructive Evaluation, Volume 30
AIP Conf. Proc. 1335, 581-588 (2011); doi: 10.1063/1.3591903

radiation, can "see through" both saw cuts quite clearly as demonstrated in the C-scan image of Fig. 2 in transmission mode.

To theoretically validate this finding as well as to build up our T-ray modeling capability, we have developed a simple measurement model. Following the same procedure as was described in [2], the signal spectrum can be expressed as a product of individual components in the frequency domain. In the case of T-ray propagation through the glass composite plate, its signal spectrum Γ_{GC} reads:

$$\Gamma_{GC}(f) = \Gamma_{air}(f) e^{-\alpha(f) L_{plate}} T(f) \tag{1}$$

$\Gamma_{air}(f)$ in Eq. (1) carries the T-ray system response via a separate thru-air measurement using exactly the same setup, L_{plate} is the plate thickness, and T(f) is the transmission coefficient. For the ½ inch plate thickness, T(f) can be approximated by the plane-wave half-space transmission coefficients:

$$T(f) \approx T_{half-space} = T_{air \to GC} T_{GC \to air} = \frac{2\eta_{GC}}{\eta_{air} + \eta_{GC}} \frac{2\eta_{air}}{\eta_{air} + \eta_{GC}} \tag{2}$$

The intrinsic impedance η_{GC} relates to material properties of the GFRP, namely, relative permeability μ_r and relative permittivity ε_r via

$$\eta_{GC} = \eta_{air} \sqrt{\frac{\mu_r}{\varepsilon_r}} \tag{3}$$

For non-magnetic materials, $\mu_r \sim 1$ and the overall ε_r can be determined by

$$\varepsilon_r = \left(1 + \frac{c\Delta t}{L_{plate}}\right)^2 \tag{4}$$

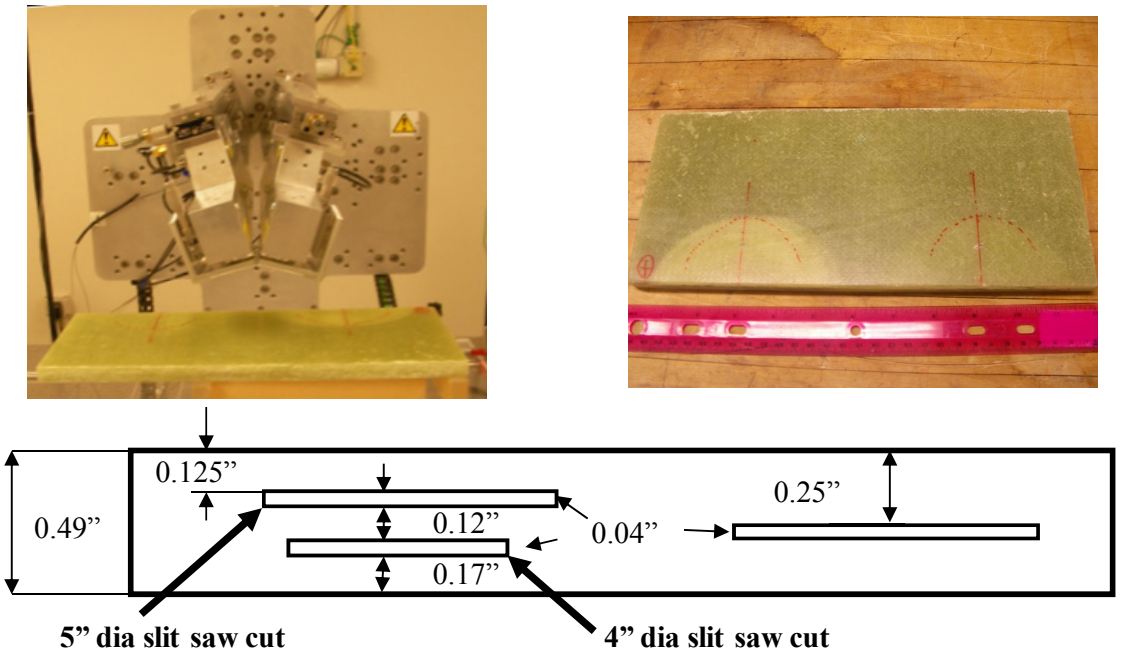

FIGURE 1. a (top left) T-ray reflection scan of the GFRP plate; **b** (top right) top view of the GFRP plate with multiple circular saw cuts; **c** (bottom) diagram showing detailed dimensions of the saw cuts.

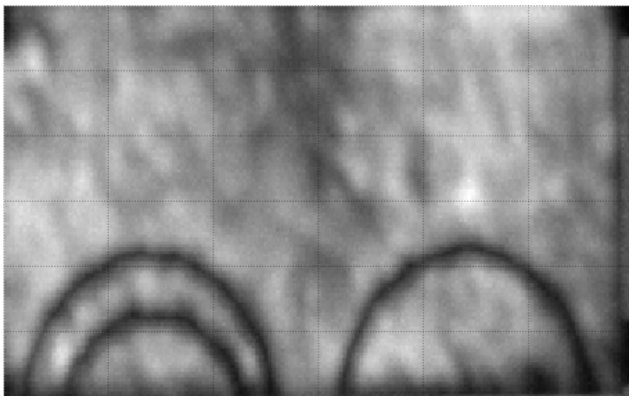

FIGURE 2. T-ray transmission C-scan image of the multiple saw cuts.

where c is the speed of light and Δt is the time-of-flight difference between the thru-air and thru-plate measurements. Lastly, α(f) denotes the attenuation constant, which can be characterized by re-arranging Eq. (1) and making use of a simple Wiener deconvolution:

$$\alpha(f) = -\frac{1}{L_{plate}} \ln\left(\frac{1}{T(f)} \frac{\Gamma_{GC}(f)}{\Gamma_{air}(f)}\right) \approx -\frac{1}{L_{plate}} \ln\left(\frac{1}{T(f)} \frac{\Gamma_{GC}\Gamma_{air}^{*}}{|\Gamma_{air}|^2 + D}\right) \qquad (5)$$

in which D is a damping (smoothing) factor relating to signal-to-noise ratio. Fig. 3 plots the attenuation constant α as a function of frequency within the range by using a damping factor 0.001 in Eq. (5).

After all unknowns are determined, Eq. (1) is readily to be extended for further modeling use. In the "hidden" delamination case, two kinds of signals are of interest. One was generated from propagating T-ray through the main areas (away from the edges) of the saw-cut, and the other was obtained by "splitting" the T-ray beam at the edge of the saw-cut, i.e. some portion of the beam traveling inside of the cut and some other outside the cut. Here we present two examples for the double saw-cut geometry, one for each kind of signal. For the former, we consider the case that the entire beam passes through both the top and the bottom saw-cuts. For the latter, we study the situation where the whole beam passes though the top cut but is split at the edge of the bottom cut.

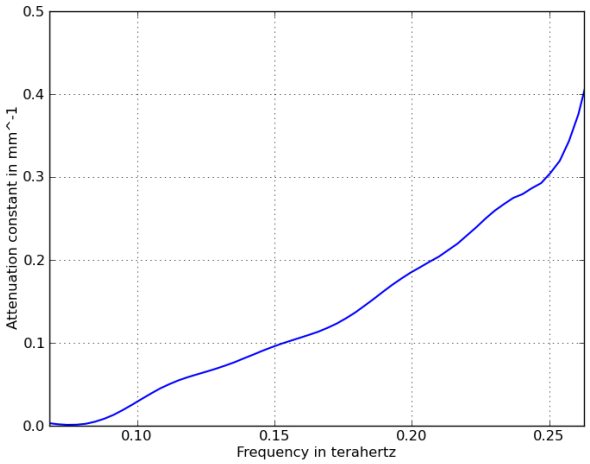

FIGURE 3. Attenuation constant estimate plotted as a function of frequency in the range by using damping factor 0.001 in the Wiener deconvolution.

In the former case, the beam path of attenuation needs to be reduced by $2L_{cut}$ to account for the "emptiness" (air gap) within the two saw-cuts. As such, Eq. (1) is modified to be:

$$\Gamma_{cuts}(f) = \Gamma_{air}(f) e^{-\alpha(f)(L_{plate}-2L_{cut})} (T_{air\to GC} T_{GC\to air})^3 \tag{6}$$

Note that the transmission coefficient term is also raised to third power to account for the six GFRP-air interfaces. Figs. 4a through 4d illustrate the geometry of beam path, the corresponding location (marked by an X) in C-scan image that the experimental waveform was sampled, and the experimental vs. model signal spectrum and waveform. As can be seen between Figs. 4c and 4d, experimental data and model prediction are in quite good agreement.

The beam splitting situation causes phase cancellation (and hence signal drop) around the edges of all three circular saw-cuts (the two double cuts on the left-hand side and the single one on the right). The signal drop can be clearly seen as dark rings around the cut edges in the C-scan image of Fig. 2. The phase cancellation is largely originated from the speed difference between T-ray propagating in the air gap within the saw-cuts and that in the GFRP. When these two signals rejoin on the same transmission path, their phases (delayed by different travel speeds) partially cancel each other, resulting in a distorted and weaker return signal (Fig. 5d). This phenomenon has been known since T-ray was introduced to detect flaws in space shuttle's spray-on form insulation structure [1,3], and has been modeled by employing a much more sophisticated technique [4]. Considering all the physics as mentioned above, we can approximated the spectrum in this situation by simply taking average of both wave components traveling inside and out of the bottom cut:

$$\Gamma_{cut-edge}(f) \approx \Gamma_{air}(f) \frac{1}{2}\Big[e^{-\alpha(f)(L_{plate}-2L_{cut})} (T_{air\to GC} T_{GC\to air})^3 e^{i(k_{GC}-k_{air})L_{cut}} + e^{-\alpha(f)(L_{plate}-L_{cut})} (T_{air\to GC} T_{GC\to air})^2 \Big] \tag{7}$$

The inside component has the same expressions as in Eq. (6) plus an exponential phase term to account for the time delay in the bottom cut. For the outside component, the path of attenuation is only reduced by one L_{cut} and transmission coefficient takes only second power for just four GFRP-air interfaces. Figs 5a-5d show similar beam path, spectrum, waveform, etc. to those in Figs. 4a-4d. Again, without getting into complicate beam calculations, our simple measurement model produces very good agreement with the experiment for the not so simple beam splitting situation.

SIMULATION OF FTIR PROPERTIES INVERSION

FTIR techniques for material characterization have been well established [5]. However, similar work in the T-ray frequency region was just being developed recently. Here we conducted an extensive simulation study to assess the feasibility of unifying both FTIR and T-ray in a common least-squares inversion scheme. The initial effort was to simulate FTIR reflection from an air-dielectric interface at oblique incidence and to determine the dielectric's electromagnetic properties such as the refractive index by using the reflection data taken at various incident angles. With sufficient thickness, the dielectric can be considered as a half-space medium. A simple uniform plane-wave model

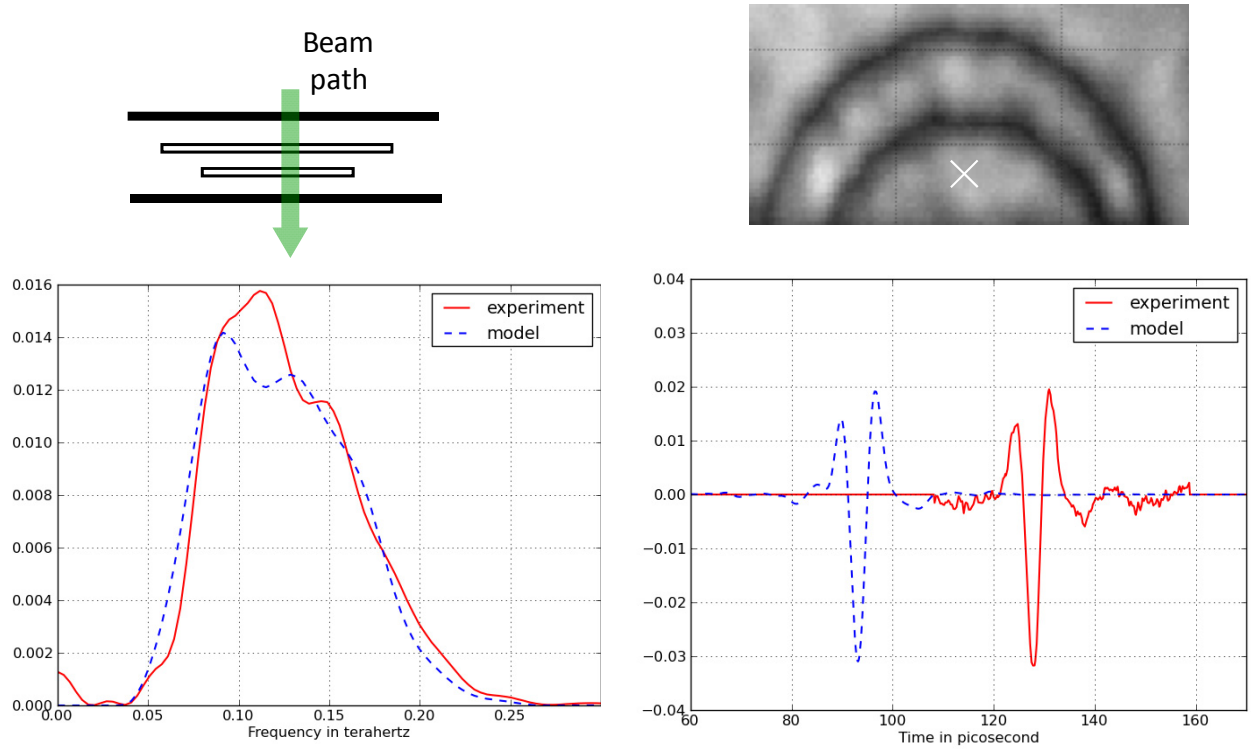

FIGURE 4. Modeling T-ray signal through the double saw-cuts: **a** (top left) the geometry of beam path; **b** (top right) the corresponding location (marked by X) in C-scan image that the experimental waveform was sampled; **c** (bottom left) the experimental vs. model spectrum; **d** (bottom right) the experimental vs. model waveform.

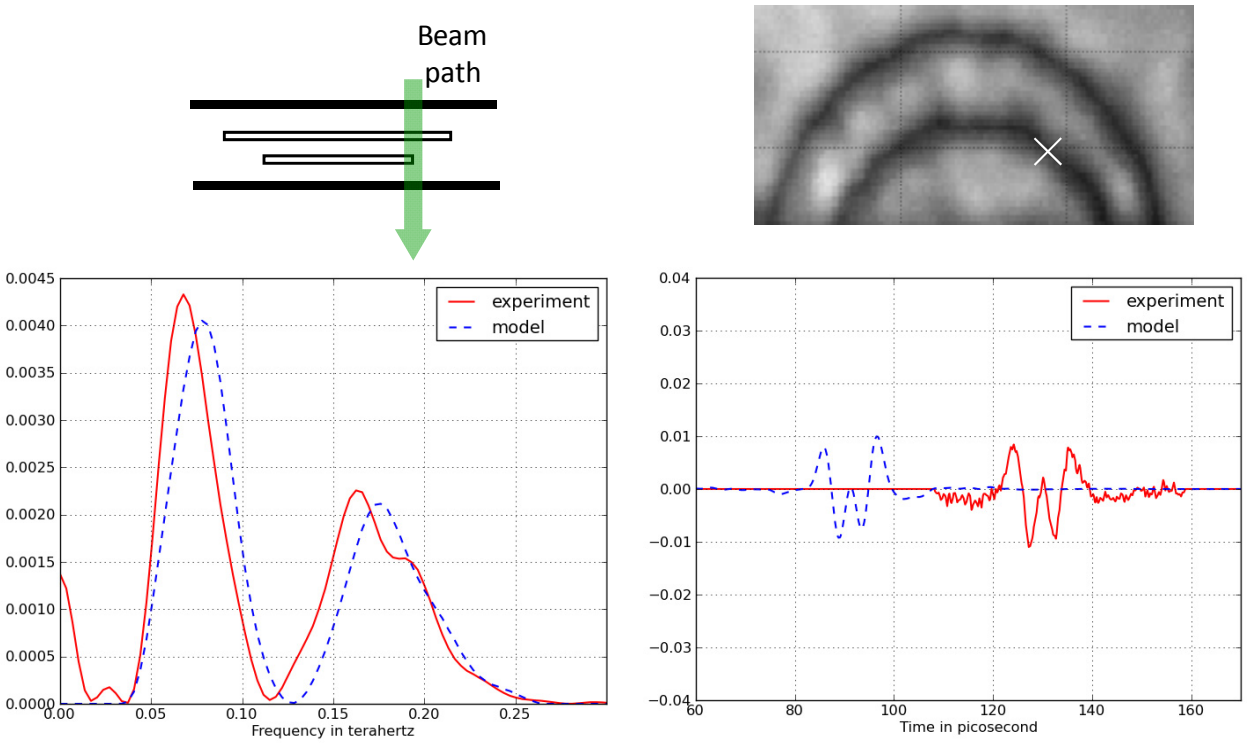

FIGURE 5. Modeling T-ray signal through the top saw-cut and the edge of bottom saw-cut: **a** (top left) the geometry of beam path; **b** (top right) the corresponding location (marked by X) in C-scan image that the experimental waveform was sampled; **c** (bottom left) the experimental vs. model spectrum; **d** (bottom right) the experimental vs. model waveform.

was then developed for such configuration involving the Fresnel equations. For an unpolarized infrared source, the irradiance (intensity) of the reflected wave consists of both parallel polarization (TM mode) and perpendicular polarization (TE mode) components as functions of both the refractive index n_d and the incident angle θ:

$$I_r(n_d,\theta) \propto A_{TE} R_{TE}^2(n_d,\theta) + A_{TM} R_{TM}^2(n_d,\theta) \tag{8}$$

in which the Fresnel reflection coefficients R_{TM} and R_{TE} are of the form (with the air refractive index taken as unity implicitly) [5]

$$R_{TM} = \frac{\left[n_d^2 - \sin^2\theta\right]^{\frac{1}{2}} - n_d^2\cos\theta}{\left[n_d^2 - \sin^2\theta\right]^{\frac{1}{2}} + n_d^2\cos\theta}; R_{TE} = \frac{\cos\theta - \left[n_d^2 - \sin^2\theta\right]^{\frac{1}{2}}}{\cos\theta + \left[n_d^2 - \sin^2\theta\right]^{\frac{1}{2}}}. \tag{9}$$

We assume a "well mixed" unpolarized source so that $A_{TE}=A_{TM}$ in Eq. (8).

Eq. (9) predicts that the absolute amplitudes of both R_{TM} and R_{TE} drop near the Brewster angle at 56.3° and approach unity at grazing angle 90°. Here the refractive index n_d is taken to be complex: $n_d = n_r + i \cdot n_i$ in which n_r is the lossless refractive index and n_i is the extinction coefficient. For glass in both cases, $n_r = 1.5$, and a value of 0.3 is used for n_i in the lossy case.

In order to remove the dependence of A_{TE} and A_{TM} in Eq. (8), we normalize all reflected irradiance $I_r(n_d, \theta)$ by that at 5° incident angle. This 5° angle is chosen to match with the configuration in the experiment where 5° is the closest possible to normal incidence. The normalized irradiances for both lossless and lossy cases remain constant at lower angle and increases rapidly approaching grazing angle.

To determine the electromagnetic properties of a dielectric like the lossless refractive index n_r and the extinction coefficient n_i here, a nonlinear least squares fitting procedure was formulated. A least squares sum $S(n_r,n_i)$ can be formed between N sets of theoretical I_r (θ_j, n_r, n_i) (Eq. (8)) and the corresponding experimental data $I_r'(\theta_j, n_r, n_i)$ measured at the N incident angle θ_i:

$$S(n_r,n_i) = \sum_{j=1}^{N}\left[I_r(\theta_j,n_r,n_i) - I_r'(\theta_j,n_r,n_i)\right]^2 \tag{10}$$

the best fitted solutions for n_r and n_i can then be found by iteratively minimizing $S(n_r,n_i)$ with an initial guess.

In this study, we simulated the experimental data $I_r'(\theta_j, n_r, n_i)$ by adding different levels of "noises" to the theoretical I_r (θ_j, n_r, n_i). The "noises" were obtained from a uniform distribution using a numerical random number generator. A total of 8 data sets from 15° to 85° at the increment of 10° were used in the least squares sum (Eq. (10)). We again considered the case of lossy glass with $n_r=1.5$ and $n_i=0.3$. For the minimization

software, we utilized a Fortran90 update of the original MINPACK-1 [6], which implemented a modified version of the popular Levenberg–Marquardt method.

Extensive numerical experiments at several controlled noise amplitude ranges were conducted. At each noise amplitude range, a total of 100 runs were made. For each run, renewed noise values were added to the theoretical I_r (θ_j, n_r, n_i) and the minimization procedure was executed 5 times, each time with a different initial guess. Figs 6 and 7 depict the deviation of the best-fit solutions from the true values of n_r and n_i vs. the several root-mean-square (RMS) noise levels. It is clear that the simulation results are quite stable, showing small deviations at linear increase with nose level. At RMS noise level nearly 0.5 which is 50% of the irradiance amplitude of lower angle data sets, the average of the worst deviations from the true extinction coefficient n_i at 0.3 is only 30%. The performance of MINPACK-1 minimization routine is also exceptional: for 90% of the 100 runs at each noise level, all 5 initial guesses converged to the same best-fit solutions, and for the remaining 10% runs, at least 4 initial guesses converged.

This FTIR inversion procedure has been tested on a family of ceramic materials related to zirconium dioxide with reasonable accurate results. We are currently extending this inversion procedure to T-ray frequency range and testing with simulated data. The ultimate goal is to develop a unified approach of connecting T-ray with FTIR in the far-infrared region of electromagnetic spectrum. We will seek for common grounds between these two techniques in many aspects, including governing physics, data processing and fusion methods.

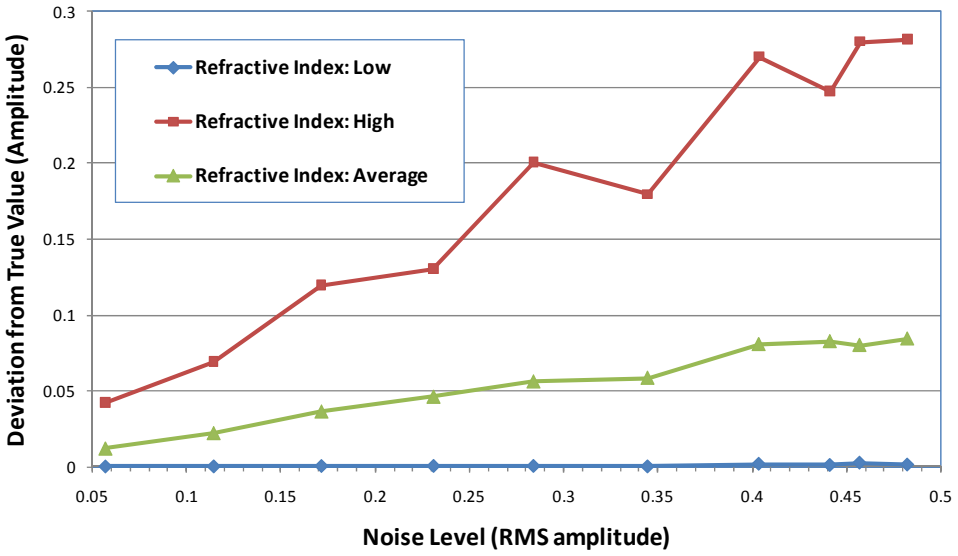

FIGURE 6. The high-average-low deviations (from the true value) of the best-fitted refractive index vs. different noise levels.

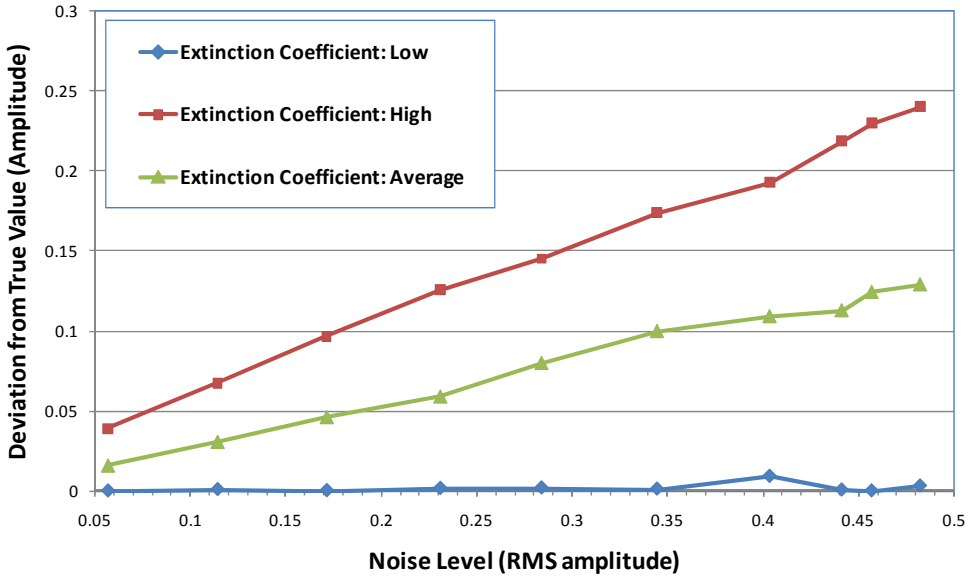

FIGURE 7. The high-average-low deviations (from the true value) of the best-fitted extinction coefficient vs. different noise levels.

ACKNOWLEDGEMENTS

This work was performed at the Center for Nondestructive Evaluation at Iowa State University with funding from the Air Force Research Laboratory through S&K Technologies, Inc. on delivery order number 5007-IOWA-001 of the prime contract F09650-00-D-0018, and from the NSF Industry/University Cooperative Research Center program. It was also supported by the Federal Aviation Administration under Contract #DTFACT-09-C-00004 and Contract #DTFA03-98-D00008, Delivery Orders IA04, technical monitor Paul Swindell. Major funding for the equipment used in this work was from the National Science Foundation Major Research Instrumentation Program under award CBET-0821556.

REFERENCES

1. D. Zimdars, J. A. Valdmanis, J. S. White, G. Stuk, S. Williamson, W. P. Winfree and E. I. Madaras, "Technology and Applications of Terahertz Imaging Non-Destructive Examination: Inspection of Space Shuttle Sprayed on Foam Insulation", Review of Progress in Quantitative Nondestructive Evaluation, D. O. Thompson and D. E. Chimenti, eds., Vol. 24A, 2005, 570-577.
2. C.-P. Chiou, R. B. Thompson and J. L. Blackshire, "Terahertz Ray System Calibration and Material Characterizations," Review of Progress in Quantitative Nondestructive Evaluation, D. O. Thompson and D. E. Chimenti eds., Vol. 28A, 2009, pp. 410-417.
3. C.-P. Chiou, R. B. Thompson, W. P. Winfree, E. I. Madaras and J. Seebo, "Modeling and Processing of Terahertz Imaging in Space Shuttle External Tank Foam Inspection," Review of Progress in Quantitative Nondestructive Evaluation, D. O. Thompson and D. E. Chimenti eds., Vol. 25A, 2006, pp. 484-491.
4. C.-P. Chiou, R. B. Thompson and J. L. Blackshire, "Modeling of Terahertz Ray Signals for NDE Applications," Review of Progress in Quantitative Nondestructive Evaluation, D. O. Thompson and D. E. Chimenti eds., Vol. 27A, 2008, pp. 414-420.
5. P R. Griffiths and J. A. De Haseth, Fourier Transform Infrared Spectrometry, 2nd Ed., Wiley-Intersicence, 2007.
6. Jorge J. More, et al., User Guide for MINPACK-1, ANL-80-74, Argonne National Lab., 1980.